

Variability in the properties of the distribution of the relative humidity with respect to ice: Implications for contrail formation

Sidiki Sanogo¹, Olivier Boucher¹, Nicolas Bellouin^{1,2}, Audran Borella¹, Kevin Wolf^{1,a}, and Susanne Rohs³

¹Institut Pierre-Simon Laplace, Sorbonne Université / CNRS, Paris, France

²Department of Meteorology, University of Reading, Reading, United Kingdom

³Forschungszentrum Jülich GmbH, Institute of Energy and Climate Research 8 – Troposphere, Jülich, Germany

^anow at Leipzig Institute for Meteorology (LIM), Leipzig University, Leipzig, Germany

Correspondence: Sidiki Sanogo (sidiki.sanogo@ipsl.fr) and Olivier Boucher (olivier.boucher@ipsl.fr)

Abstract.

Relative humidity with respect to ice (RHi) is a key variable in the formation of cirrus clouds and contrails. We document its probability density function (PDF) using long-term Measurement of OZone and water vapour on AIrbus In-service airCraft programme (MOZAIC) and the In-service Aircraft for a Global Observing System (IAGOS) observations over the period

5 1995–2022 in the upper troposphere (UT) and lower stratosphere (LS) between 325 hPa and 175 hPa. The characteristics of the RHi PDF differ in the UT and in LS of the high-latitudes (HL) and mid-latitudes (ML) regions of the Northern Hemisphere. In the LS, this PDF decreases exponentially with increasing RHi. In the UT, it first increases exponentially in subsaturated conditions then decreases exponentially in supersaturated conditions. Because of these different behaviours, the PDF for the combined UT and LS is bimodal. In contrast to the HL and the ML regions, the RHi PDF in the tropical troposphere decreases 10 exponentially with increasing RHi. The different forms of PDF, in the tropics and in the higher latitude regions, lead to a global PDF of RHi in subsaturated tropospheric conditions that is almost uniform. These findings invite caution when using MOZAIC and IAGOS measurements to calibrate large-scale simulations of RHi. The variability of RHi properties associated with that of temperature also has implications for the formation of contrails. We examined the impact of switching fuel (from kerosene to bio-ethanol or liquid-hydrogen) on the frequency of contrail formation using the Schmidt-Appleman criterion. We show 15 that bio-ethanol and to a larger extent liquid-hydrogen would produce more contrails. The impact of a potential change from kerosene to these alternative fuels decreases with decreasing pressure but increases when moving from the high-latitudes of the Northern Hemisphere to the tropics. Finally, we emphasize that investigations of the impact on contrail occurrence frequency of switching from fossil kerosene to more sustainable fuels must be carried out in various meteorological conditions.

1 Introduction

20 Water vapour in the Earth’s atmosphere is responsible for two-thirds of the natural greenhouse effect (Peixoto and Oort, 1992). It plays an important role in the transport of energy from the Earth’s surface into the atmosphere via evapotranspiration of water at the ground and condensation and freezing in the atmosphere (Gierens et al., 2012). A convenient variable to analyze

the condensation and freezing processes at play in in-situ cirrus clouds and contrails formation is the Relative Humidity with respect to ice (RHi). Situations where RHi is 100 % are said to be "saturated with respect to ice". It is common for water 25 vapour to be ice supersaturated ($RHi > 100\%$) in the upper troposphere (UT) and lower stratosphere (LS), but also in the lower troposphere in Antarctica (Gierens et al., 1999; Gierens and Brinkop, 2012; Genthon et al., 2017; Petzold et al., 2020).

Ice supersaturation occurrence is a prerequisite for the formation of in-situ natural cirrus and persistent contrails (Schumann, 1996; Heymsfield et al., 2017). In-situ cirrus clouds may form in the UT and in the LS via homogeneous nucleation at temperature colder than $-38\text{ }^{\circ}\text{C}$ and RHi above 140 % is then necessary (Heymsfield et al., 2017; Kanji et al., 2017). Cirrus clouds 30 may also form via heterogeneous freezing at temperatures lower than $0\text{ }^{\circ}\text{C}$ with RHi above 100 % in the presence of ice nucleating particles (Heymsfield et al., 2017; Kanji et al., 2017). The formation mechanism of contrails is quite different to those of natural cirrus. Contrails are linked to the atmospheric conditions that influence the complex processes occurring in the wake of aircraft (Schumann, 1996; Kärcher, 2018). Schmidt (1941) and Appleman (1953) provided a simple thermodynamic criterion, 35 known as the Schmidt–Appleman criterion (SAC), which approximates the complex dynamical processes and is based only on ambient temperature and relative humidity. It has been amended by Schumann (1996), taking into account fuel combustion properties and the aircraft engine propulsion efficiency (see Section 2.4 for a refresher on the criterion).

Contrails can evolve into ice clouds, known as contrail-cirrus (Kärcher, 2018). Like natural cirrus, contrail-cirrus have a radiative forcing that is of relevance to the Earth's climate (Kärcher, 2018; Lee et al., 2021; Schumann et al., 2021). They interact with both solar and terrestrial radiation and the net effect is a warming of the climate system (Lee et al., 2021). However, 40 there is a large spread in the net radiative forcing for individual contrail-cirrus and the average magnitude of this effect is still uncertain. For instance, for the year 2018, the Effective Radiative Forcing (ERF) of contrail-cirrus in high-humidity regions was estimated to be 57.4 mW m^{-2} with a 5-95 % likelihood range of 17 to 98 mW m^{-2} (Lee et al., 2021). This non-CO₂ forcing of aviation might be stronger than that from CO₂ (34.3 mW m^{-2} with a 5-95 % likelihood range of 31 to 38 mW m^{-2}) (Lee et al., 2021). Overall, the uncertainty associated with the ERF of contrails and contrail-cirrus represents a significant part of the 45 uncertainty associated with the total ERF of aviation on the Earth's climate (Lee et al., 2021). A further uncertainty regarding the climate impact of contrail-cirrus relates to their efficacy in warming the Earth's surface. Some studies (e.g., Ponater et al., 2021; Bickel, 2023) suggest that their efficacy might be lower than 1, meaning that contrail radiative forcing may be less efficient at causing surface temperature change than CO₂ radiative forcing.

Accurate representation of Ice SuperSaturation Regions (ISSR) in numerical weather prediction models is important to 50 improve the prediction of persistent contrails, which is important for mitigation strategies aiming to reduce the climate impact of the aviation sector through contrail avoidance (Sperber and Gierens, 2023). This requires a good characterization of the spatial and temporal distribution of RHi. For this purpose, the characterization of ISSR (corresponding to the upper tail of the RHi distribution) has been carried out in past studies (e.g., Gierens et al., 1999; Petzold et al., 2020). The frequency of occurrence of ISSR has been shown to depend on the location and season. In terms of spatial variability, the highest frequency 55 is observed in deep convection regions in the tropics above 200 hPa (Spichtinger et al., 2003a, b; Lamquin et al., 2012). ISSR are more frequent at 300-200 hPa and 400-300 hPa in the mid and high-latitude regions, respectively (Lamquin et al., 2012). In terms of seasonality, the highest frequency of occurrence in the Northern Hemisphere mid-latitude regions is observed in winter,

followed by spring, while they are less frequent in summer and autumn (Petzold et al., 2020; Wolf et al., 2023). On a global scale, the seasonality of ISSR frequency shows spatial disparities depending on pressure level (see Fig. 10 in Lamquin et al. 60 (2012)). It should be noted that the magnitude of the ISSR frequency of occurrence depends on the observational products being considered (e.g., airborne or spaceborne observations) due to differences in observation methods and their horizontal and vertical resolutions. Analysis using the European research programme MOZAIC showed that, on average in the troposphere an aircraft above 300 hPa has a 20-30 % and 35-40 % probability of encountering an ISSR in summer and in winter respectively, when flying over North America, the North Atlantic and Europe (Petzold et al., 2020). So, the average spatial distribution of 65 ISSR is fairly well documented in the literature. However, the occurrence of contrails also depends on the ambient temperature, the fuel combustion properties and the engine propulsion efficiency (Schumann, 1996).

The Probability Density Function (PDF) of RHi has also been analysed in several studies (e.g., Lamquin et al., 2012; Diao et al., 2014; Smit et al., 2014; Petzold et al., 2020) based on in situ measurements. They all found a bimodal PDF with a first mode between 0 and 10 % and a second mode between 95 and 112 %. However, there is still a gap in our knowledge of the 70 properties of the tropospheric and stratospheric PDFs of RHi. Gierens et al. (1999) showed that the large scale PDF of RHi in the UT and LS are different at 250 and 200 hPa. The PDF of RHi in the LS follows an exponential decay both below and above saturation, and therefore does not show any break in slope in the vicinity of 100 %, unlike in the UT. A contradicting findings of Spichtinger et al. (2003a), indicate that the RHi PDF in the LS exhibits a break in slope in the vicinity of 100 % 75 over the location of Lindenberg (Germany) using radiosonde observations. The question of how these properties vary between the tropics and the mid and high-latitudes regions, and also with pressure, has so far not been fully answered.

In this context, the objectives of this study are twofold: 1) to document the properties of the PDF of RHi in the UT and in the LS, in both clear and cloudy conditions as a function of latitude and pressure, 2) to document the frequency of occurrence of conditions favorable to the formation of non-persistent and persistent contrails and the impact of a fuel change on these frequencies using the Schmidt-Appleman criterion.

80 This article is structured as follows. Section 2 details the dataset used in the study and describes our methodology. Section 3 documents the properties of the PDF of RHi and the frequency of occurrence of the conditions favorable to contrail formation. Finally, Section 4 summarizes our main findings.

2 Data and methods

2.1 Dataset from IAGOS and MOZAIC passenger aircraft

85 We analyzed RHi from airborne measurements for the period 1995 to 2022. Measurements of ambient temperature (T) and pressure (p), relative humidity with respect to liquid water (RHi), ozone volume mixing ratio (m_{O_3}), and ice crystal number concentration (N_i) are also analysed either to understand the properties of the PDF of RHi or to document the frequency of the conditions favorable to the formation of contrails. They are all obtained from the Measurement of OZone and water vapour on 90 Airbus In-service airCraft (MOZAIC) programme (Marenco et al., 1998) over the period 1995-2014 and from the In-service Aircraft for a Global Observing System (IAGOS) programme (Petzold et al., 2015) over the period 2011-2022. Data for N_i are

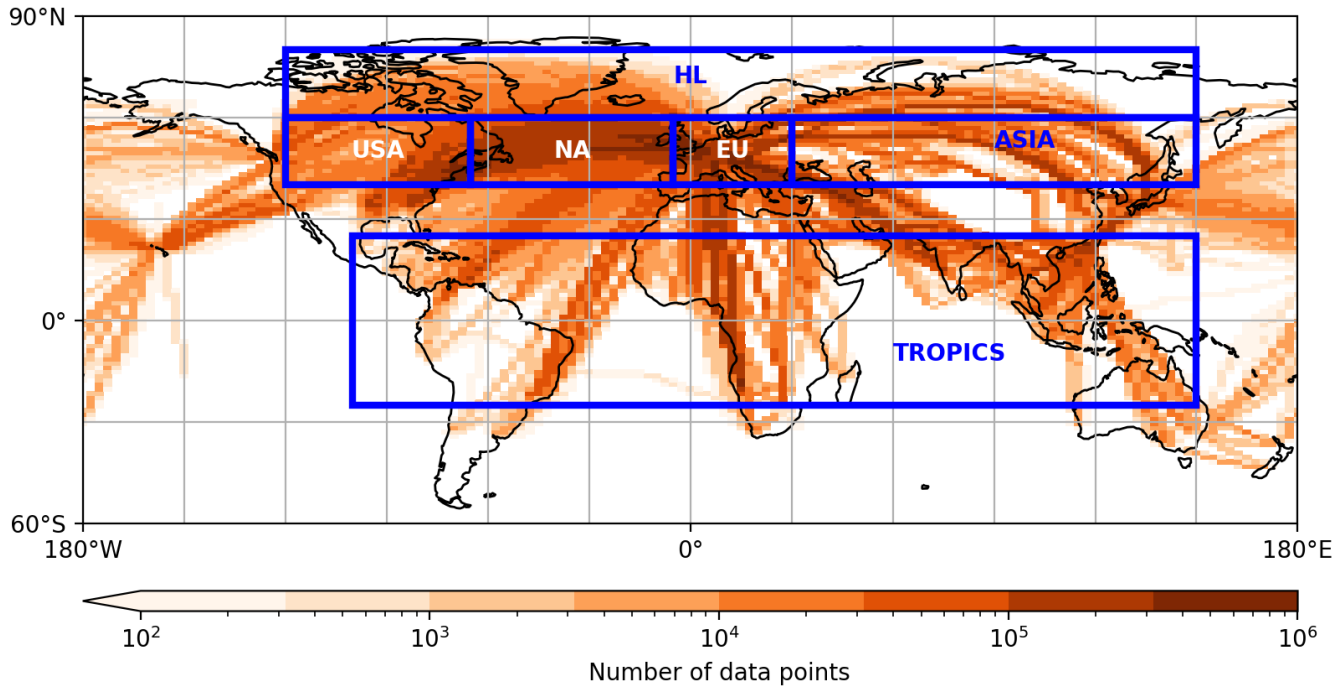


Figure 1. Global coverage of RH_i observations by MOZAIC and IAGOS aircraft over the 1995-2022 period, between 325 and 175 hPa shown as the total number of measurements per $2.5^\circ \times 2.5^\circ$ gridbox (log scale). The areas delimited by blue boxes represent the study areas. Their coordinates are provided in Table 1.

available only from a subset of the IAGOS flights. The MOZAIC and IAGOS data are measured with a temporal sampling of 4 seconds. In this study, for each flight we used the latest version (file version 3.1.1 to 3.1.4) available at the time of our study.

Figure 1 shows the spatio-temporal distribution of RH_i measurements in the Upper Troposphere - Lower Stratosphere (UTLS) defined here as the pressure layer between 325 and 175 hPa. The best sampled areas are in the Mid-Latitudes (ML) of the Northern Hemisphere. They are the United States of America ($40^\circ\text{N} - 60^\circ\text{N}$, $120^\circ\text{W} - 65^\circ\text{W}$, USA hereafter), Europe ($40^\circ\text{N} - 60^\circ\text{N}$, $5^\circ\text{W} - 30^\circ\text{E}$, EU hereafter) and especially the North Atlantic corridor ($40^\circ\text{N} - 60^\circ\text{N}$, $65^\circ\text{W} - 5^\circ\text{W}$, NA hereafter). Sampling over Russia, Asia, the High-Latitudes (HL) of the Northern Hemisphere and in the tropics is less dense. Our study is focused on the HL, ML, and the tropics. The area of the ML in a longitude range from the USA to Europe is analysed in more detail. The geographical coordinates of the different study areas are provided in Table 1. For documenting the PDF of RH_i, we considered data above 325 hPa by splitting the UTLS into three layers 325-275 hPa, 275-225 hPa and 225-175 hPa using a resolution of 50 hPa. Most measurements are performed in the 275-225 hPa and 225-175 hPa layers (Fig. 2). Those performed in 325-275 hPa are less numerous (Fig. 2) but they represent 186812, 4963539, 2980377 measurements in the HL, the ML, and in the tropics, respectively.

Table 1. Names of study areas and their geographical coordinates.

Study areas	Latitude and longitude ranges
High-Latitudes (HL)	60°N – 80°N, 120°W – 150°E
Mid-Latitudes (ML)	40°N – 60°N, 120°W – 150°E
United States of America (USA)	40°N – 60°N, 105°W – 65°W
North Atlantic (NA)	40°N – 60°N, 65°W – 5°W
Europe (EU)	40°N – 60°N, 5°W – 30°E
Tropics	25°S – 25°N, 100°W – 150°E

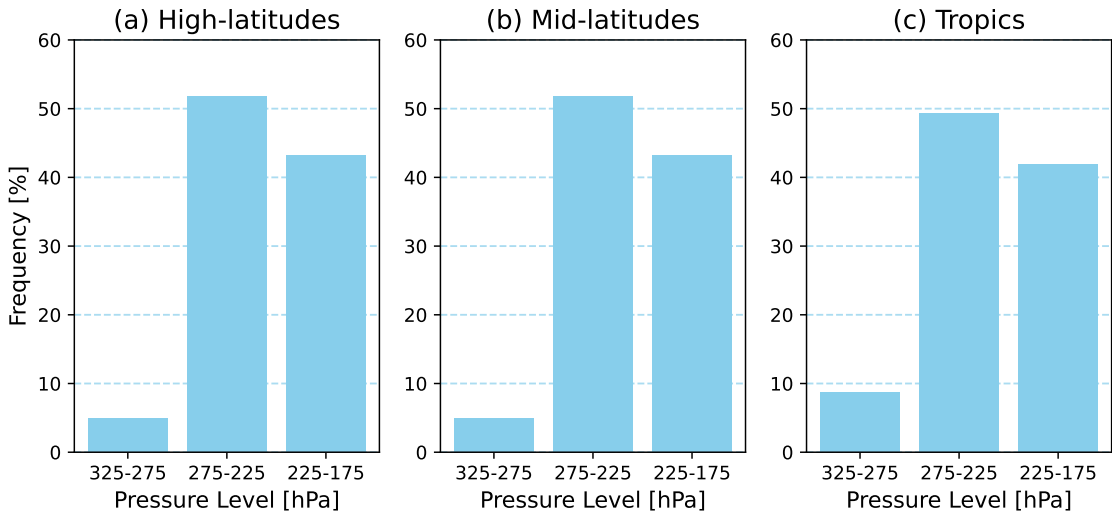


Figure 2. Relative frequency of RHi measurements per pressure layer in a) the high-latitudes, b) the mid-latitudes of the Northern Hemisphere and c) the tropics over the period 1995–2022.

2.2 Data selection

105 MOZAIC and IAGOS data are assigned different quality levels, ranging from "good" to "not validated". In this study, only "good" measurements of RHi, RHI, T , p , m_{03} , and N_i are considered. It should be noted that, between the years 2011 and 2017, there was a grounding problem with the IAGOS data acquisition system. For this period, the quality flag of RHi is not well derived but it is known to be similar to that of RHI. We therefore selected RHi values using the RHI quality flag for this particular period. We follow Gierens et al. (1999) by separating UT and LS air mass measurements on the basis of their m_{03} .

110 The mean value of the ozone mixing ratio m_{03} at the thermal tropopause being 130 ppb with a standard deviation of 92 ppb (Duhnke et al., 1998), we consider that measurements are from a UT air mass if $m_{03} < 130$ ppb and an LS air mass otherwise. This approach is used for a comparison of our results to those of Gierens et al. (1999). A sensitivity analysis using the threshold of 2 potential vorticity units as simulated by the fifth generation of the European Centre for Medium-Range Weather Forecasts

atmospheric reanalysis (ERA5) to discriminate tropospheric and stratospheric measurements showed consistent results with

115 the m_{0_3} based approach (not shown).

2.3 Differentiation of clear sky and cloudy conditions

The N_i variable is used to differentiate observations measured in cirrus clouds from those in clear sky conditions. Different

thresholds are used in the literature. For instance, Beswick et al. (2015) and Lloyd et al. (2020) used a threshold of 0.05 particles

cm^{-3} while Petzold et al. (2017) used a lower threshold of 0.015 particles cm^{-3} . Here we used an even smaller threshold

120 of 0.001 particles cm^{-3} , i.e, we considered cloud measurements to have $N_i \geq 0.001 \text{ particles cm}^{-3}$. We used this threshold

to be more restrictive in the discrimination of the clear conditions for the investigations of the origin of the wet mode in the

PDF of RHi. We then perform a sensitivity test with thresholds of 0.015 particles cm^{-3} and 0.05 particles cm^{-3} since the

threshold of 0.001 cm^{-3} is associated with detection uncertainties that can exceed 50 % (Petzold et al., 2017). To exclude

125 potential measurements in the presence of supercooled liquid water, as in Petzold et al. (2017), we considered only N_i data

for which the temperature is colder than -40°C , which corresponds to the threshold for the homogeneous freezing of water

droplets (Petzold et al., 2017). Because of low sampling of the HL by IAGOS aircraft equipped with N_i measurement sensors,

the analysis involving screening clear and cloudy conditions is restricted only to the ML and to the tropics.

2.4 Contrail detection: Schmidt-Appleman criterion

The combustion of kerosene (or alternative fuels) releases hot and humid air behind the aircraft, which is progressively diluted

130 in the cold and dry ambient atmosphere. This mixture follows a line in a $p - T$ diagram (Schumann, 1996). In this framework,

contrails form at ambient temperature below a critical value T_{crit} and RHi larger than RHi_{crit} (Schumann, 1996). We used

this criterion known as SAc to document the frequency of non-persistent and persistent contrails formation as a function of the

pressure for the following fuels: kerosene, bio-ethanol (ethanol, hereafter) and liquid-hydrogen (hydrogen, hereafter). Contrails

are persistent if RHi is above 100% (See Fig. 3 in Schumann, 1996).

135 The approximation of T_{crit} frequently used in the literature (e.g., Rap et al., 2010) is given by the following equation:

$$T_{crit} = 226.69 + 9.43 \cdot \ln(G - 0.053) + 0.7272 \cdot \ln^2(G - 0.053) \quad (1)$$

where G (in Pa K^{-1}) is the slope of the mixture line in the $p - T$ diagram and is defined as follows:

$$G = \frac{EI_{H_2O} \cdot c_p \cdot p}{\epsilon \cdot Q(1 - \eta)} \quad (2)$$

G combines the atmospheric properties (the ambient pressure (in Pa) of the flight altitude, the isobaric heat capacity of air

140 $c_p = 1004 \text{ J kg}^{-1} \text{ K}^{-1}$, and the ratio of the molecular masses of water vapour and dry air $\epsilon \approx 0.622$), the fuel properties (the

specific combustion heat of the fuel Q (in J kg^{-1}) and the emission index of water vapour for the fuels EI_{H_2O} (in kg kg^{-1}))

and the aircraft engine propulsion efficiency of the aircraft η . In this study, we consider $\eta = 0.3$ which corresponds to a typical

present-day fleet value (Schumann, 1996, 2012). The values of Q and EI_{H_2O} for the different fuels are listed in Schumann

(1996) and in Wolf et al. (2023).

145 The RHl_{crit} threshold for an ambient temperature T is determined by:

$$RHl_{crit} = \frac{G \cdot (T - T_{crit}) + e_{sat}^{liq}(T_{crit})}{e_{sat}^{liq}(T)} \quad (3)$$

where e_{sat}^{liq} is the saturation water vapour pressure. For more details, the reader should refer to Schumann (1996) and Rap et al. (2010).

3 Results

150 3.1 Number of ice crystals in cirrus clouds

Situations that are ice supersaturated and subsaturated are observed in both clear and cloudy conditions (Kahn et al., 2009; Krämer et al., 2009, 2016; Petzold et al., 2017). Therefore, for a better characterization of the PDF of RHi, we first document how clear and cloudy conditions are sampled in IAGOS measurements. For this purpose, we used three different detection thresholds (0.001, 0.015, 0.05 particles cm^{-3}) for characterizing clouds, based on their ice crystal number concentration N_i 155 (see Section 2.3). We found, consistently with Petzold et al. (2017), that IAGOS aircraft encounter cirrus clouds with larger N_i in the tropics than in the ML (Fig. 3). Considering only non-zero N_i values, the percentages of datapoints above the thresholds of 0.015 (0.05) particles cm^{-3} are 63 (47) % and 56 (40) % for the 275-225 and 225-175 hPa layers, respectively in the tropics (Fig. 3). In the ML, the percentages are 58 (38) % for the 325-275 hPa layer, 40 (20) % for the 275-225 hPa layer (Fig. 3). The highest fraction of $N_i < 0.015 \text{ cm}^{-3}$ in ML is observed at the altitudes of 225-175 hPa, with a value of 72 % (Fig. 3). 160 The higher N_i in cirrus clouds in the tropics compared to the ML between 275-175 hPa is consistent with the findings of studies using synergistic lidar-radar satellite data (e.g., Sourdeval et al., 2018) and can be explained by the fact that, in the tropical region, strong updrafts in convective regions produce ice supersaturation and cause high nucleation rates that lead to high number concentrations of ice crystals (Krämer et al., 2016).

Table 2. Number of datapoints (with ambient temperature lower than -40°C) including a measurement of the ice crystals number concentration (N_i) and percentage of datapoints for which $N_i \geq 0.001, 0.015, 0.05 \text{ particles cm}^{-3}$ in the mid-latitudes (ML) of the Northern Hemisphere and in the tropics over the period 2011-2022.

Regions	Mid-latitudes			Tropics	
Pressure ranges (hPa)	325-275	275-225	225-175	275-225	225-175
Total number of datapoints with $T < -40^\circ\text{C}$	155620	2905616	4402016	1539032	4502899
Fraction of datapoints ($N_i \geq 0.001 \text{ particles cm}^{-3}$)	6.0 %	3.7 %	1.8 %	4.4 %	8.2 %
Fraction of datapoints ($N_i \geq 0.015 \text{ particles cm}^{-3}$)	3.5 %	1.4 %	0.5 %	2.7 %	4.6 %
Fraction of datapoints ($N_i \geq 0.05 \text{ particles cm}^{-3}$)	2.0 %	0.7 %	0.2 %	2.0 %	3.3 %

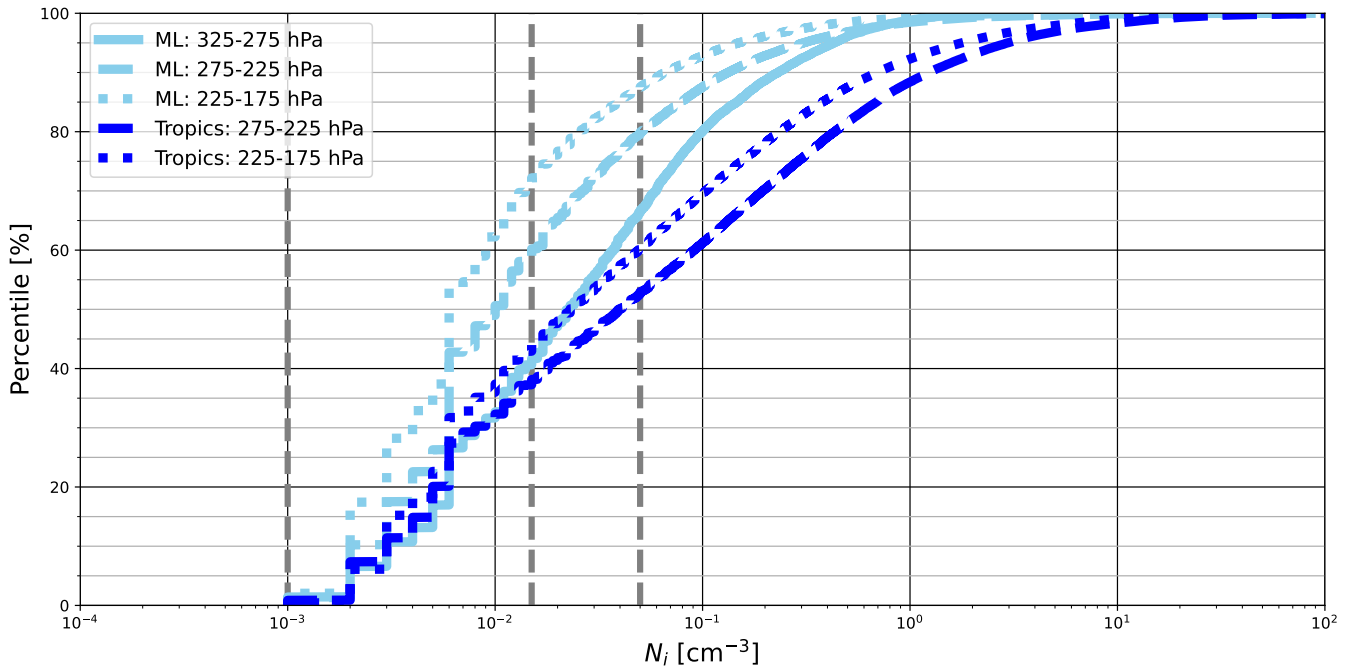


Figure 3. Cumulative PDF of the ice crystal number concentrations in the mid-latitudes (ML) of the Northern Hemisphere and in the tropics over the period 2011–2022 for different pressure layers. The vertical dashed gray lines correspond to the concentration thresholds of 0.001 , 0.015 and 0.05 cm^{-3} (see Text).

3.2 How often do IAGOS aircraft fly in cirrus clouds?

165 The fractions of aircraft flying time in cirrus clouds are presented in Table 2. They are computed for each pressure layer as the number of measurements of N_i collocated with measurements of temperature lower than -40 $^{\circ}\text{C}$ that are at least equal to the cirrus detection threshold divided by the total number of measurements. These fractions can also be interpreted as cirrus occurrence frequencies as seen by IAGOS. The occurrence frequency of cirrus clouds decreases in the ML with decreasing pressure (when going from 275–225 to 225–175 hPa) while it increases in the tropics. Using $0.001 \text{ particles cm}^{-3}$ as a
 170 threshold, we determined fractions of 4.4% and 8.2% in the tropics and 3.7 % to 1.8 % in the ML (Table 2). On average, the total occurrence frequency of cirrus is highest in the tropics (Table 2). This is consistent with the findings of Petzold et al. (2017) who showed that IAGOS data capture the global pattern of cirrus clouds. When the detection threshold is increased to $0.015 \text{ particles cm}^{-3}$ and $0.05 \text{ particles cm}^{-3}$, cirrus cloud occurrence frequency decreases, in particular in the 225–175 hPa layer (Table 2), but remains large. This suggests that the properties of RHi PDF from MOZAIC and IAGOS measurements
 175 correspond to a combination of clear-sky and cloudy-sky conditions.

3.3 Characteristics of the RHi probability density function

3.3.1 Upper troposphere

Gierens et al. (1999) showed that over larger spatial scales and longer time scales, the distributions of RHi smaller and larger than 100 % in the UT follow a uniform law and an exponential law, respectively. RHi is however modulated in space and time 180 by fluctuations in specific humidity and temperature (Diao et al., 2014). Consequently, its statistical distribution is subject to spatial variability. This is illustrated in Fig. 4 that shows the PDF of RHi in the ML, the HL and in the tropics, for the 325-275, 275-225 and 225-175 hPa pressure layers. In the ML, the characteristics of the RHi PDF depend on the pressure level. It is unimodal in 325-275 hPa with a mode at 108 % (Fig. 4d) while it is bimodal in the 275-225 and 225-175 hPa layers. The two modes in 275-225 hPa are centered at 5 % and 108 % (Fig. 4e) while those in 225-175 hPa are located at 8 % and 100 % 185 (Fig. 4f). The existence or the magnitude of the dry mode in the 275-225 and 225-175 hPa layers in the ML is not certain. It may correspond to LS measurements, erroneously attributed to the UT because of uncertainties in the method for discriminating UT and LS measurements of RHi. We therefore focused the following analysis on the RHi values greater than 25 %. The presence of a wet mode was reported in the study of Spichtinger et al. (2003a) based on radiosoundings over Lindenberg (Germany). In agreement with Reutter et al. (2020) who analyzed RHi in the North Atlantic, the mean and the standard deviation of RHi 190 distributions in the UT vary little with the pressure level in the ML (Table 3). However, their variations are substantial in the tropical and HL regions (Table 3).

An important point, common to these UT RHi distributions and consistently with Gierens et al. (1999), is that the PDF decreases exponentially with increasing RHi beyond a value S (here, $S \in [100 \%, 110 \%]$). For a quantitative intercomparison of the part of the RHi PDF corresponding to $\text{RHi} \geq S$, we take $S = 100 \%$, and as Gierens et al. (1999), we fit each PDF using 195 the following straight line:

$$\ln(PDF) \approx a + b \cdot \text{RHi} \quad (4)$$

in which a is the intercept and b is the slope. For the three different pressure layers, b (multiplied by 100 for legibility) is close to -4 and a is between 2 and 3 in the ML (Table 4). The PDF has different characteristics in the range of RHi that correspond to subsaturation. The PDF of $\text{RHi} \in [25 \%, 100 \%]$ increases ($b \geq 0$), instead of decreasing exponentially with 200 increasing RHi in the 275-225 and 225-175 hPa layers (Table 4). In the 325-275 hPa layer, the PDF is nearly uniform ($b \approx 0$) for $\text{RHi} \in [25 \%, 100 \%]$ (Table 4). The comparison of USA, North Atlantic, and Europe reveals that, in the first order, the distributions of RHi over the three regions are consistent with each other in the 275-225 and 225-175 hPa layers (Fig. 5). However, substantial differences appear in the 325-275 hPa layer. The magnitude of the dry mode at these pressure levels is higher in the USA compared to the other two areas (Fig. 5), for all seasons (see Fig. S1 in the Supplementary Material). 205 In addition, the PDF of RHi between 25 % and 100 % is almost uniform over Europe, while it increases and decreases exponentially over the North Atlantic and USA, respectively (Fig. 5). This implies differences between the three sub-regions in the mechanisms that modulate RHi variability in the pressure range 325-275 hPa. Insufficient sampling may also be a contributing factor, since fewer measurements were made at these pressure levels (Fig. 2). The UT RHi PDFs in the HL

exhibit similar features to those in the ML (Fig. 4a-c). However, for RHi between 25 % and 100 %, the exponential rate of
210 increase b is slightly higher for the HL than for the ML (Fig. 4a-f, Table 4).

In the tropical region, the evolution of the RHi PDF with pressure is different (Fig. 4g-i). The PDFs are bimodal and in
contrast to the ML and the HL, the magnitude of the dry mode increases with increasing pressure (i.e going down in the
atmosphere) while that of the wet mode increases. This is due to the warm tropical temperatures, which favour low RHi for
325-275 hPa despite the higher availability of water vapour compared to the other two pressure layers considered here. Unlike
215 the ML and the HL, the existence of a mode between 0 and 25 % is more certain in the tropics since the measurements analyzed
are less affected by stratospheric measurements. For RHi ≥ 25 %, the PDF is characterised by an exponential decay on both
sides of the mode at 100 %. The characteristics of the PDF above 100 % are similar to those of the RHi PDF in the ML and HL.
The important difference is that the absolute value of the rate parameter b decreases with decreasing pressure in the tropics,
whereas it increases in ML and HL (Table 4). It is worth noting that the global PDF (PDF combining RHi measurements in
220 HL, ML and tropics) includes opposing tendencies in the PDF of RHi lower than 100 % between the tropics and the Northern
Hemisphere, resulting in an almost uniform PDF ($b \approx 0$, Fig. 4j-l). These results are consistent with the findings of Gierens
et al. (1999).

Table 3. Long-term (1995-2022) mean and standard deviation of the RHI values in the UT (and in the LS) in the High and Mid-Latitudes of the North Hemisphere and in the tropics.

RHi PDF parameters		Mean (%)			Standard deviation (%)		
Regions		High-Latitudes	Mid-Latitudes	Tropics	High-Latitudes	Mid-Latitudes	Tropics
325 - 275 hPa		88.9 (33.0)	71.5 (31.3)	27.0	38.6 (23.9)	33.7 (23.1)	35.2
275 - 225 hPa		48.6 (24.4)	78.4 (28.4)	34.2	48.6 (23.7)	32.2 (25.4)	18.8
225 - 175 hPa		56.9 (30.7)	69.8 (24.5)	38.8	56.9 (22.5)	36.4 (24.7)	33.8

Table 4. Values (with uncertainty range of ± 1 standard deviation) of the parameters a and b of the fit lines (see Eq. 4) in the supersaturated (top) and subsaturated (bottom) part of the RHi distribution in the UT, computed over the period 1995-2022. The values of b are multiplied by 100 for the sake of legibility.

Fit parameters	a				$100 \cdot b$		
	Regions	High-Latitudes	Mid-Latitudes	Tropics	High-Latitudes	Mid-Latitudes	Tropics
325 - 275 hPa	2.3 ± 0.24	2.1 ± 0.12	4.3 ± 0.48	-3.7 ± 0.18	-3.7 ± 0.09	-6.1 ± 0.04	
	-2.9 ± 0.04	-2.0 ± 0.01	-1.9 ± 0.02	1.21 ± 0.07	0.00 ± 0.01	-0.45 ± 0.00	
275 - 225 hPa	2.7 ± 0.16	2.3 ± 0.10	3.7 ± 0.18	-4.1 ± 0.011	-3.8 ± 0.07	-5.4 ± 0.04	
	-2.7 ± 0.01	-2.4 ± 0.01	-1.8 ± 0.02	0.09 ± 0.01	0.06 ± 0.02	-0.48 ± 0.00	
225 - 175 hPa	3.8 ± 0.29	2.7 ± 0.13	2.0 ± 0.09	-5.1 ± 0.21	-4.3 ± 0.01	-3.9 ± 0.04	
	-2.7 ± 0.02	-2.4 ± 0.00	-1.8 ± 0.01	0.08 ± 0.03	0.04 ± 0.00	-0.41 ± 0.00	

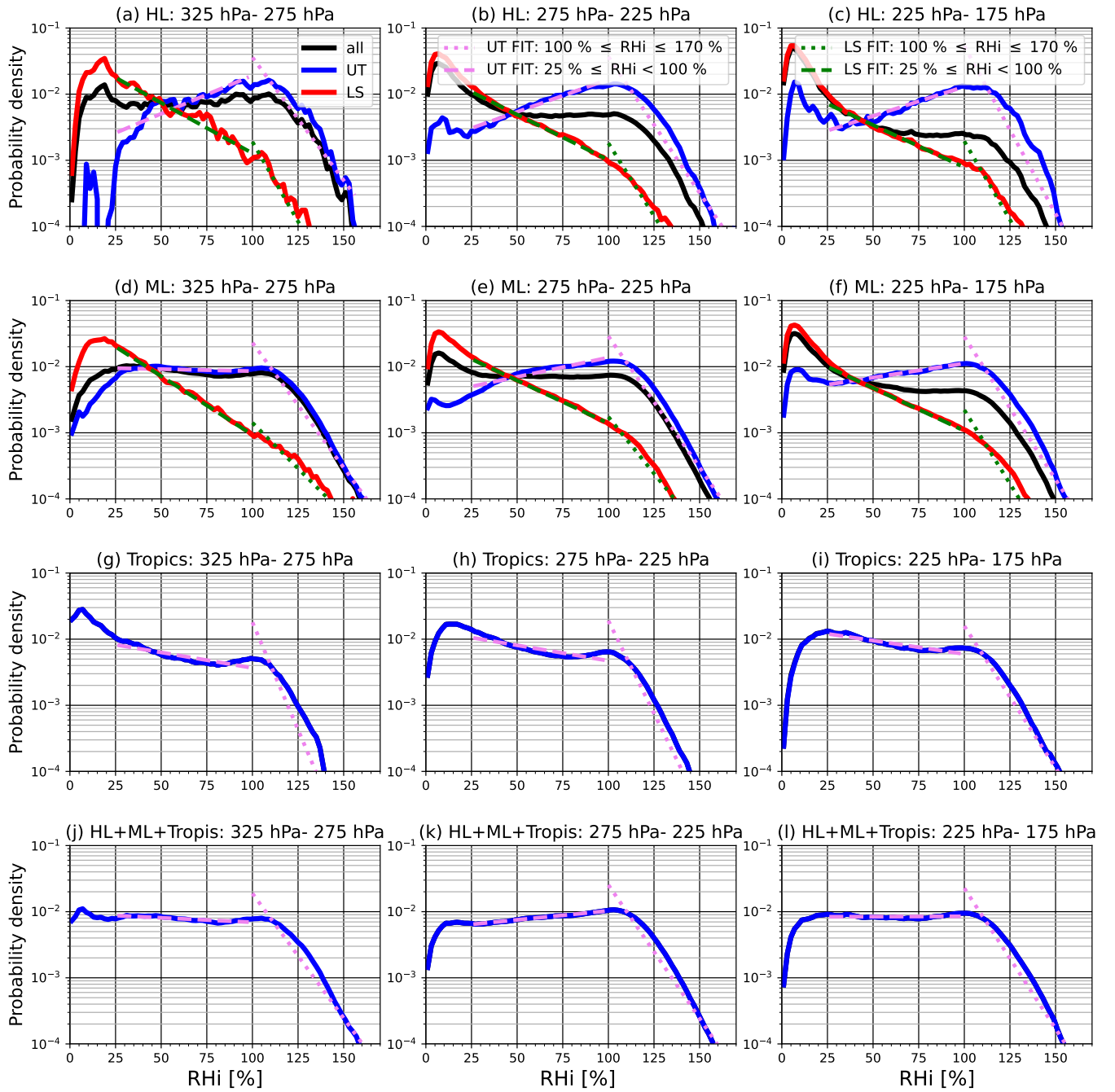


Figure 4. Probability density function of the relative humidity with respect to ice (in %) computed over the period 1995-2022 for the pressure layers 325-275, 275-225 and 225-175 hPa, a-c) in the High-Latitudes (HL) of the Northern Hemisphere, d-f) in the Mid-Latitudes (ML) of the Northern Hemisphere, g-i) for the tropical region, j-l) the PDF of the three domains combined. For each pressure layer, the tropospheric RHi PDF (blue), the stratospheric RHi PDF (red) and their combined PDF (black) are shown. The green dashed and dotted lines correspond to the fit for $\text{RHi} \in [25\%, 100\%]$ and for $\text{RHi} \in [100\%, 170\%]$, respectively, in the stratosphere. The pink dashed and dotted lines are those for the troposphere.

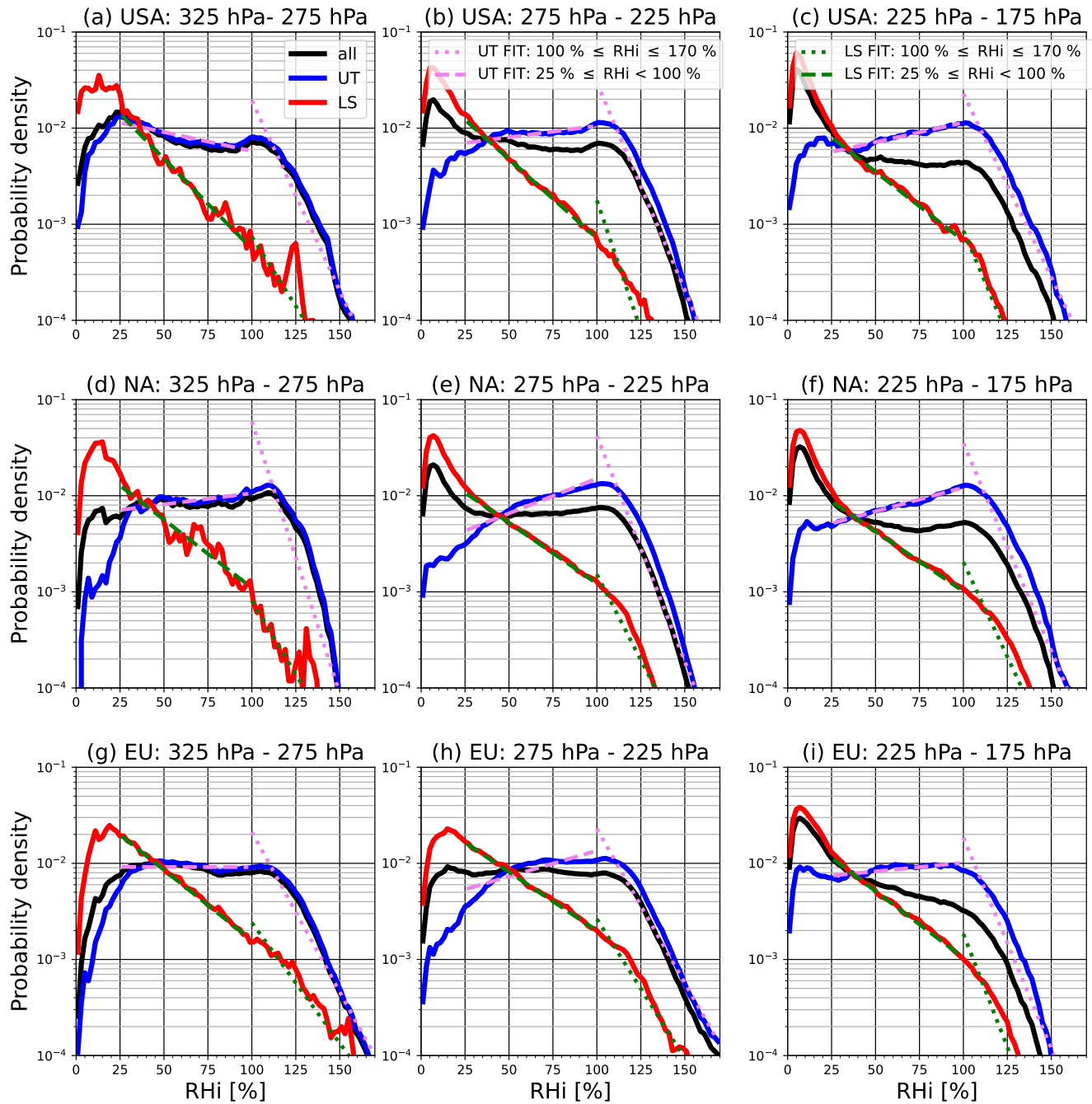


Figure 5. Same as Fig. 4 but for the North America (USA), the North Atlantic (NA), and Europe (EU).

3.3.2 Lower stratosphere

In this section, we document the RHi PDF in the LS. This analysis is carried out only in the ML and the HL because in MOZAIC 225 and IAGOS stratospheric measurements are very few in the 325-175 hPa layer in the tropics. The mean RHi decreases with decreasing pressure in the ML and HL while its standard deviation varies very little (Table 3). Reutter et al. (2020) found similar results over the North Atlantic Ocean.

The observed temperature in the UT and the LS are relatively close, but water vapour transport into the LS through the tropopause is low (Petzold et al., 2020; Reutter et al., 2020). This makes the mean value of RHi lower in the LS than in the 230 UT. Another important difference between the LS and the UT, common to the ML and the HL and to the three pressure layers considered here, is that in the LS, the PDF of RHi greater than 25 % decreases exponentially with increasing RHi (Fig. 4a-f, Table 5). This exponentially decaying PDF of RHi in the LS, with a break in the slope around 100 %, is a feature reported by Spichtinger et al. (2003a) over Lindenberg (Germany). Our results show that this property is common to the RHi PDF in the ML and the HL of the Northern Hemisphere in the 275-225 and 225-175 hPa layers (Fig. 4b,c,e,f). For these pressure layers, 235 Gierens et al. (1999) did not find the break in slope around 100 % in the MOZAIC data for the period 1995-1997. This might be due to an undersampling of the LS properties of RHi PDF over the period they considered. It is worth noting that in the 325-275 hPa layer, the break in slope around 100 % in the RHi PDF in the LS is marked only in the HL (Fig. 4a). In the ML, the break in slope seems to be undersampled in the USA in the MOZAIC and IAGOS data (Fig. 5a). In the LS, unlike the UT, the dry mode between 0 % and 25 % is expected due to the low water vapour content (see Petzold et al. (2020)).

Table 5. Same as Table 4 but for the LS.

Fit parameters	<i>a</i>		$100 \cdot b$		
	Regions	High-Latitudes	Mid-Latitudes	High-Latitudes	Mid-Latitudes
325 - 275 hPa	1.2 ± 0.34	-0.2 ± 0.09	-4.0 ± 0.29	-2.6 ± 0.06	
	-1.3 ± 0.03	-1.2 ± 0.01	-1.5 ± 0.05	-1.8 ± 0.01	
275 - 225 hPa	1.4 ± 0.16	0.8 ± 0.04	-4.1 ± 0.12	-3.6 ± 0.04	
	-1.6 ± 0.00	-1.5 ± 0.04	-1.3 ± 0.01	-1.3 ± 0.00	
225 - 175 hPa	1.7 ± 0.18	1.8 ± 0.13	-4.4 ± 0.14	-4.4 ± 0.09	
	-1.8 ± 0.01	-1.8 ± 0.01	-1.2 ± 0.02	-1.2 ± 0.01	

240 3.3.3 Lower stratosphere and upper troposphere

As shown above, there are differences between the shapes of RHi PDF in the UT and in LS in the HL and in the ML. In this section, we analyzed the properties that emerge when UT and LS are considered together. Such an approach is used in several studies (e.g., Lamquin et al., 2012; Smit et al., 2014; Diao et al., 2014; Petzold et al., 2020). We found, in agreement with these 245 studies that the RHi PDF in the UTLS is bimodal (Fig. 4a-f). The mode of the RHi PDF between 0 % and ~ 50 % (depending on pressure layer and region) is essentially a characteristic of the LS while that for RHi greater than ~ 50 % is dominated by

the features of the RHi PDF in the UT (Fig. 4a-f). The magnitude of the dry mode varies with the pressure level. It increases when going up from 325 to 175 hPa in the LS (Fig. 4a-f) since at these pressure levels in the LS, water vapour decreases while the temperature increases (Reutter et al., 2020; Petzold et al., 2020). The RHi PDF of the ML includes more UT measurements than the RHi PDF of the HL since the pressure level of the tropopause increases (i.e. its altitude decreases) with latitude.

250 Consequently, the shape of the upper tail of the RHi PDF is more dominated by the tropospheric PDF in the ML than in the HL (Fig. 4). In the ML, some differences can be noted at the sub-regional scale on the shape of the RHi PDF. The exact ranges of the lower/upper tail of the PDF of RHi dominated by the LS/UT features depend on the location (Fig. 5).

3.3.4 Clear vs cloudy conditions

To further document the RHi PDF, we compared its properties in clear and cirrus cloud conditions between 325-175 hPa in the 255 ML and in the tropics using the sub-sample of data measured onboard aircraft equipped with ice crystal number concentration measuring sensor. In these two regions, the aforementioned wet mode, in the vicinity of 100 % in the RHi PDF that combines clear and cloudy conditions appears to come essentially from cirrus clouds (Fig. 6). Conditions with $N_i < 0.001$ particles cm^{-3} associated with the slow and complex processes of cirrus clouds formation and dissipation may also contribute. Consequently, this mode also partly appears in clear sky conditions depending on the region. In the subsample of the IAGOS data analysed 260 here, it is more prominent in the tropics than in the ML (Fig. 6a-c). Petzold et al. (2017) conducted similar analyses in different regions including, areas in the tropics and ML regions using IAGOS data of the period from July 2014 to October 2015. They found that the RHi wet mode in the tropical Atlantic is more prominent (see their Fig. 8b). This characteristic seems to be smoothed out in satellite and radar-lidar synergistic data, since Kahn et al. (2009) and Lamquin et al. (2012) reported no mode in the vicinity of 100% under clear conditions.

265 In addition to the mode around 100 %, the PDF of in-cloud RHi also shows a dry mode between 0 and 50 % (Fig. 6a,c) which could correspond to a measurement artifact. The positions of the mode around 100 % are different between the ML and the tropics (Fig. 6a-c). It is subsaturated in the tropics while it is supersaturated in the ML (Fig. 6a-b). Cirrus clouds can exhibit ice subsaturated and ice supersaturated conditions depending on the stage of their life cycle (Petzold et al., 2020; Li et al., 2023). Some studies (e.g., Krämer et al., 2009; Petzold et al., 2017) have found that the mode of the PDF of RHi in cirrus 270 clouds is ice supersaturated while others (e.g., Kahn et al., 2009; Ovarlez et al., 2002; Li et al., 2023) found an ice subsaturated mode. Since the magnitude and position of this wet mode depend on the region as illustrated in this study and reported in the literature, further studies are needed to better characterize it and elucidate the mechanisms involved.

The PDF of in-cloud RHi decreases for subsaturated conditions but increases for supersaturated conditions when increasing the detection threshold (Fig. 6). This is consistent with the fact that, more generally, high concentrations of ice crystals are associated with high RHi (Petzold et al., 2017; Krämer et al., 2016). The lower tail of the PDF of RHi could include measurements in contrails or at the bottom of cirrus clouds where subsaturated conditions are observed more often (Dekoutsidis et al., 2023). They may also correspond to measurements carried out in diluted cirrus clouds or in the proximity of cirrus clouds where ice crystals may be mixed with clear air by turbulence. Erroneous measurements may also contribute since the uncertainties associated with these thresholds are large (more than 50 % for the threshold of 0.001 cm^{-3} particles, see Section 2.3).

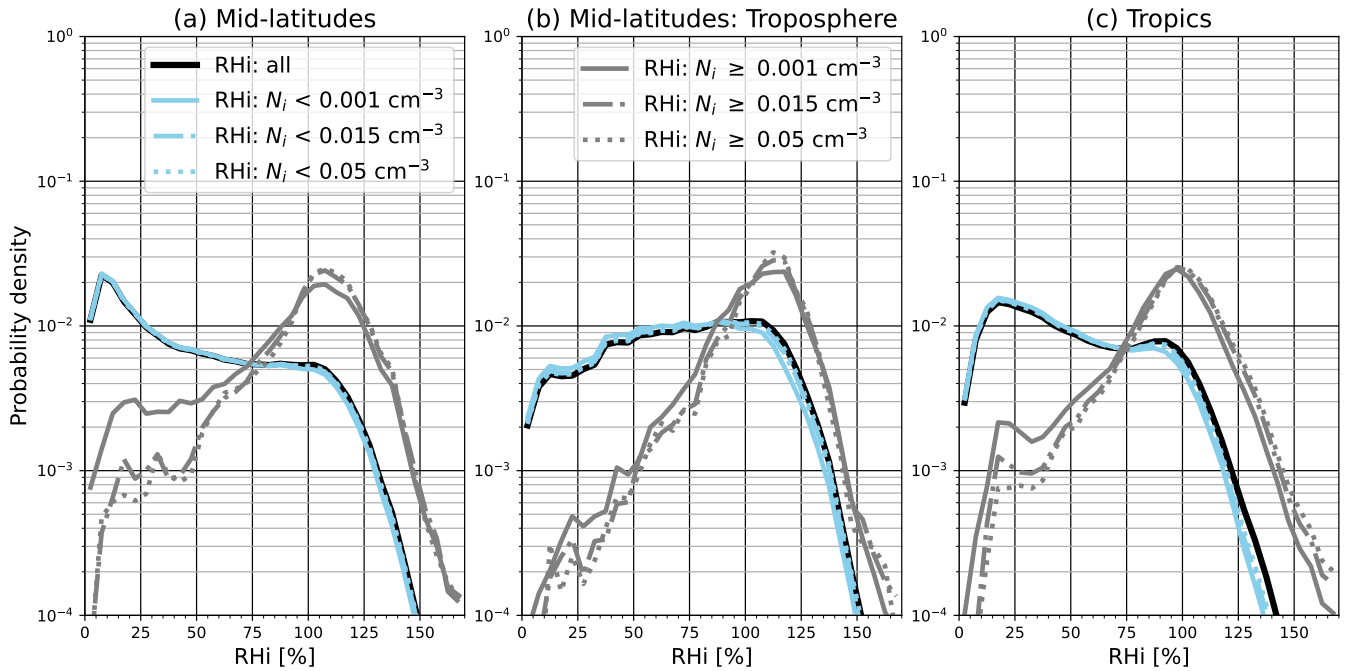


Figure 6. Probability density function of RHi in clear (sky blue) and cloudy (gray), and in all-sky (black) conditions, a) in the upper troposphere and lower stratosphere in the mid-latitudes of the Northern Hemisphere, b) only in the upper troposphere in the mid-latitudes of the Northern Hemisphere and c) in the tropical upper troposphere and lower stratosphere, computed over the period 2011-2022. Only RHi measurements collocated with measurements of temperature lower than -40°C are used in the analysis.

280 3.4 Implications of RHi variability for contrail formation

3.4.1 Frequency of ice supersaturation regions

In this section, we investigate the frequency of occurrence of ISSR, which are necessary for persistent contrail formation (Schmidt, 1941; Appleman, 1953). We computed this frequency as the ratio of aircraft flight time in ISSR to total flight time. The frequency of ISSR collocated with measurements of temperature lower than -38°C (temperatures at which cirrus clouds 285 may form by homogeneous nucleation, see Section 1) is presented in Fig. 7 while that with no restriction on the temperature is presented in Fig. 8. The difference between these two frequencies is low (less than 3 %) except for the 325-275 hPa layer in the tropics, where it is relatively high (6 %). In the HL and in the ML, ISSR frequency decreases with the pressure level (Fig. 8a-c). In the HL, for the 325-275, 275-225, 225-175 hPa layers, the occurrence frequencies of ISSR with no restriction on the temperature are respectively 19.2 %, 11.0 %, 5.5 %, while they are 21 %, 17.8 % and 9.0 % in the ML. In the tropics, 290 ISSR occur more frequently (15.6 % of the time) in the 225-175 hPa layer. In the 325-275 and 275-225 hPa layers they occur 8 % and 10.4 % of the time, respectively. It should be noted that, for the three regions, the frequency of ISSR is characterized by regional and seasonal variability. In the tropics (for the 325-275, 275-225, 225-175 hPa layers) and in the ML (for the 325-

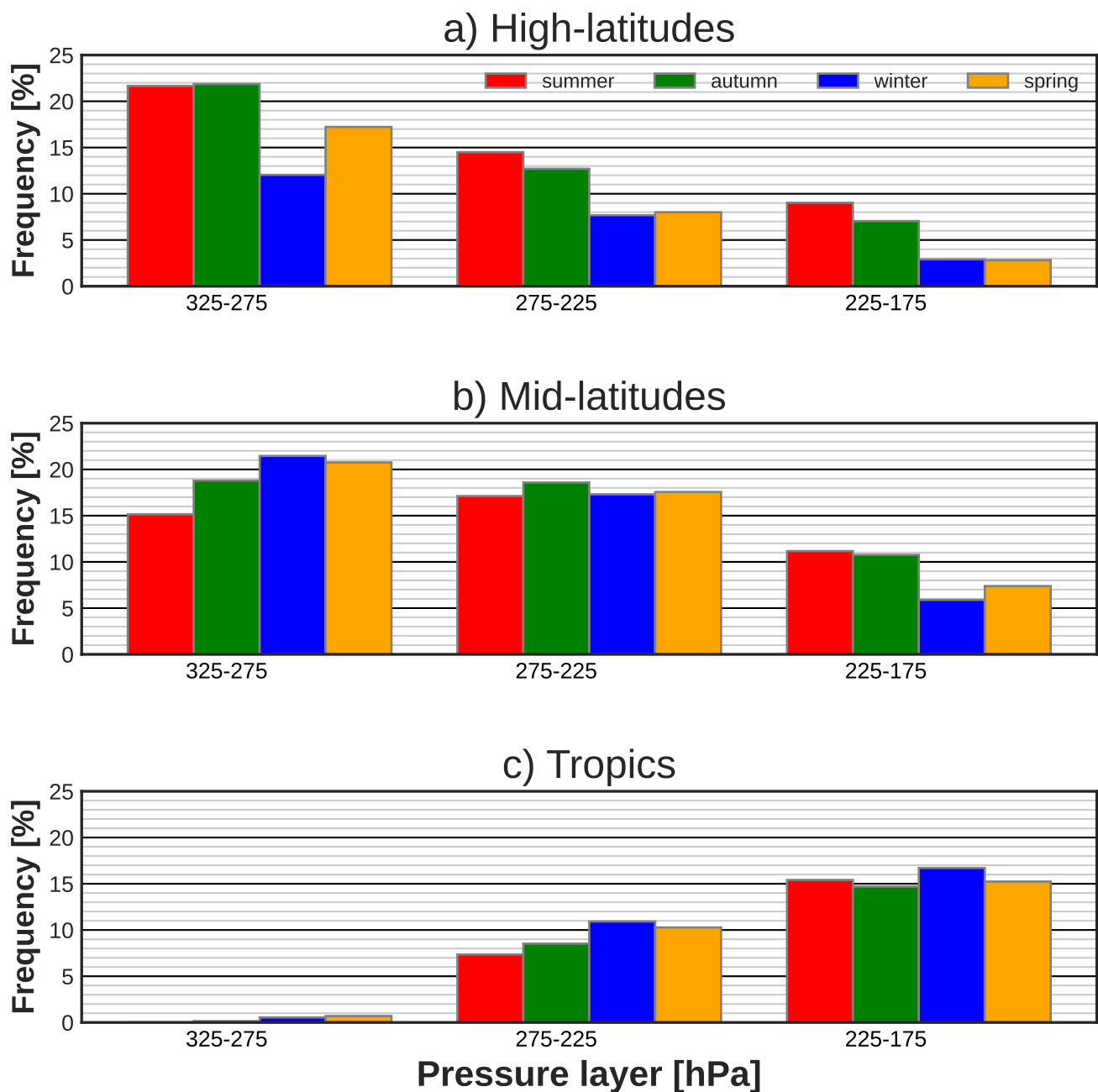


Figure 7. Frequency of ISSR (in %) for four seasons (color bars) and three pressure layers when considering only measurements with temperature lower than -38°C for a) the high and b) the mid-latitudes of the Northern Hemisphere c) and the tropics.

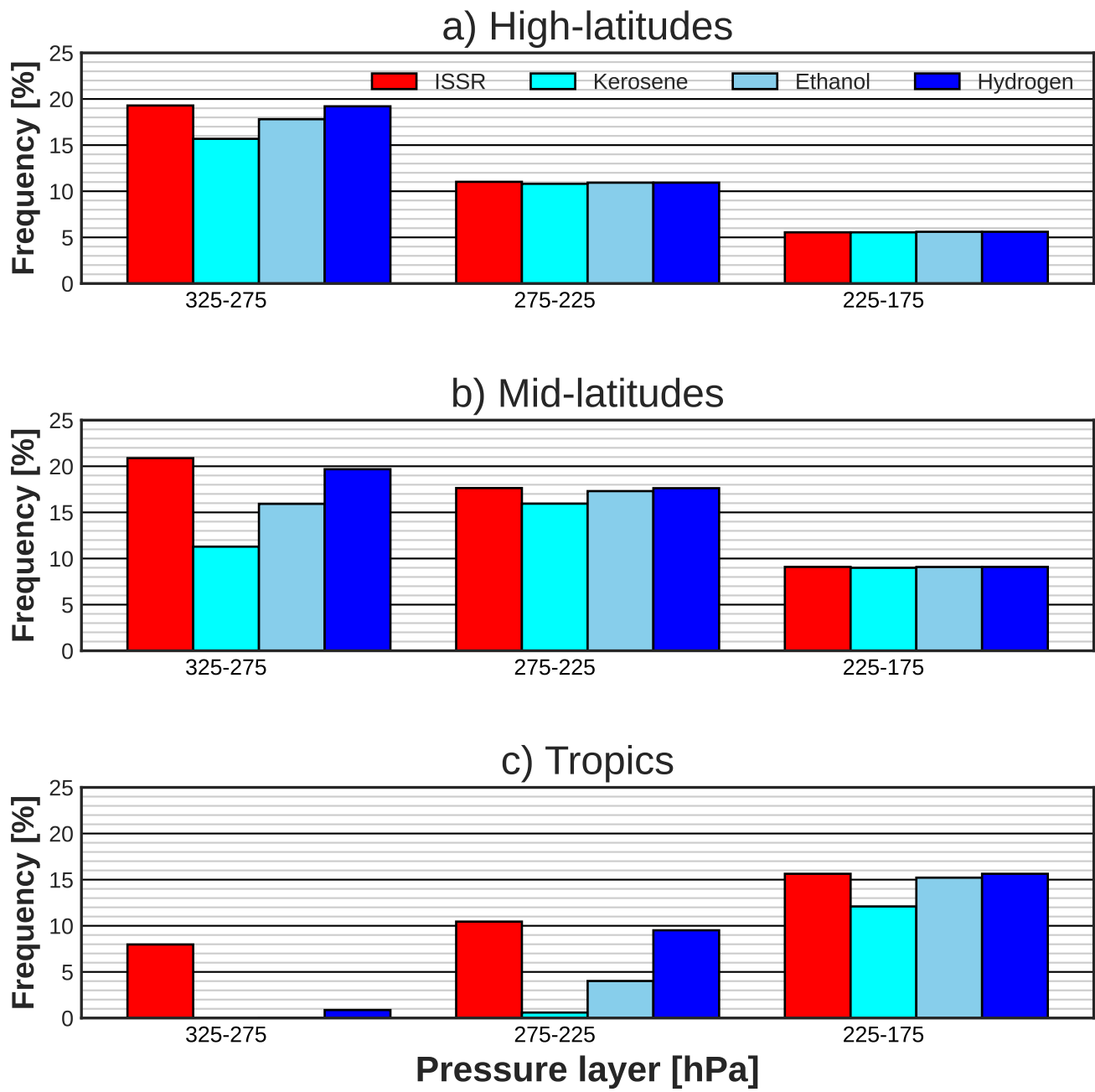


Figure 8. Annual average frequency (%) of ISSR (red) and of persistent contrail formation conditions for three pressure layers for kerosene (cyan), bio-ethanol (sky blue) and liquid-hydrogen (blue) fuels over the a) high and b) mid-latitudes of the Northern Hemisphere and over c) the tropics.

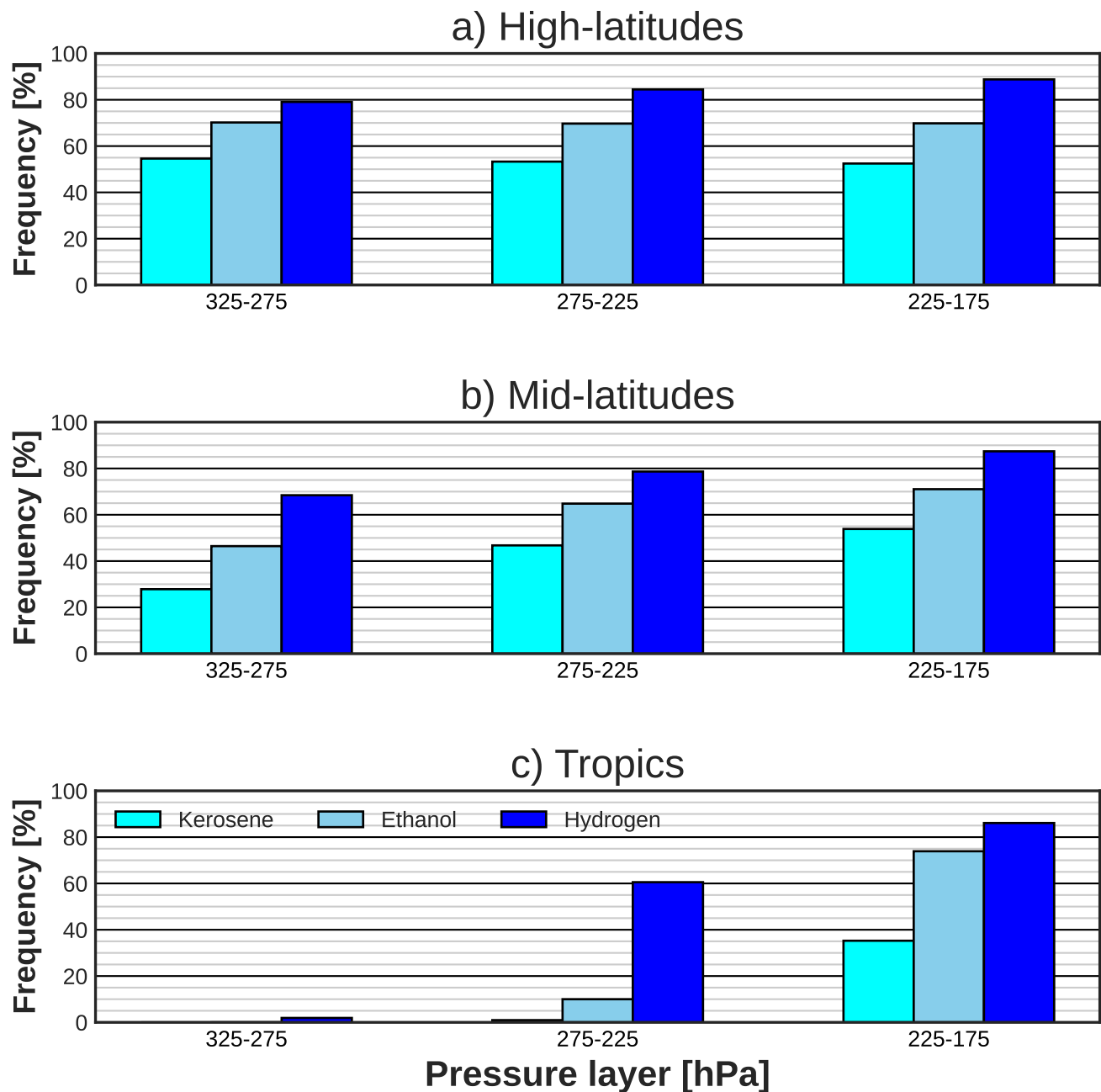


Figure 9. Annual average frequency (%) of non-persistent contrail formation conditions for three pressure layers for kerosene (cyan), bio-ethanol (sky blue) and liquid-hydrogen (blue) fuels over the a) high and b) mid-latitudes of the Northern Hemisphere and over c) the tropics.

275 hPa layer), MOZAIC and IAGOS aircraft flying time in the ISSR is highest in winter and lowest in summer (Fig. 7b-c). In the three pressure layers in the HL and for the 225-175 hPa layer in the ML, the frequency of ISSR seems to be essentially 295 driven by the seasonal evolution of LS conditions (Fig. 7a-b; see also Fig. S2), which are drier than UT conditions. In the Northern Hemisphere, the altitude of the tropopause is lower in winter and spring than in summer and autumn (Liu et al., 2014). As a result, LS air masses are sampled by MOZAIC and IAGOS aircraft more frequently in winter and spring than in summer and autumn (Fig. S2). In the 275-225 hPa layer in the ML, the seasonality of ISSR frequency is less marked (Fig. 7b). In the 325-275 hPa layer, ISSR seasonality seems to follow that of temperature (Fig. 7b). In line with Lamquin et al. (2012) 300 findings, the seasonality of ISSR frequency combining tropospheric and stratospheric conditions varies as a function of latitude and pressure.

3.4.2 Frequency of contrail formation and fuel choice

Investigations are being carried out by the aviation industry about the possibility of using bio-ethanol (ethanol, hereafter) and 305 liquid-hydrogen (hydrogen, hereafter) as alternative fuels to kerosene. Ethanol and hydrogen are two fuels that could qualify as sustainable aviation fuel, and whose use is expected to reduce aviation-induced CO₂ emissions if they are generated from carbon-neutral sources (Ng et al., 2021). They could however produce contrails which have a net warming effect on the climate (see Section 1). Here, we used the SAc to test the impact of using ethanol or hydrogen on the formation of contrails compared to kerosene. The SAc also accounts for the aircraft-engine propulsion efficiency η (see Section 2.4) which is expected to continue 310 to increase in the future (Sahoo et al., 2020). But, since our study is focused only on the impact of fuel choice, we used a typical present-day aircraft-engine propulsion efficiency of 0.3. The SAc is applied to MOZAIC and IAGOS measurements, varying the specific combustion heat of the fuel Q and the emission index of water vapour for the EI_{H_2O} of kerosene, ethanol, and hydrogen. The values of Q and EI_{H_2O} are set to 43.2 MJ kg⁻¹ and 1.25 kg kg⁻¹ for kerosene, to 27.2 MJ kg⁻¹ and 1.17 kg kg⁻¹ for ethanol, to 120 MJ kg⁻¹ and 8.94 kg kg⁻¹ for hydrogen (Schumann, 1996; Wolf et al., 2023).

The fraction of flying time during which aircraft can produce persistent contrails as a function of the fuel used is shown 315 in the Fig. 8. These fractions or frequencies depend on the region and the altitude of the flight. For instance, MOZAIC and IAGOS aircraft using kerosene and flying in the HL in the 325-275 hPa pressure layer are estimated to have produced persistent contrails during 15.8 % of the flight time (Fig. 8a). This frequency decreases to 11 % and to 5.5 % for the 275-225 and 225-175 hPa layers, respectively. For the 325-275 hPa layer, MOZAIC and IAGOS aircraft would have formed persistent contrails more often if they had used hydrogen or ethanol (19.2 % and 18 %, respectively) instead of kerosene, while the fuel used 320 has almost no effect for the 225-175 hPa layer (Fig. 8a). Comparing ISSR frequency shows that for the 325-275 hPa layer, aircraft that use kerosene fly in ice supersaturated air masses for 3.4 % of the time without producing persistent contrails. This frequency is equal to 1.2 % for ethanol and 0 % for hydrogen indicating that with hydrogen fuel, persistent contrails would form as soon as air masses are ice supersaturated. The impact of the fuel choice is much weaker for the 275-225 hPa and 225-175 hPa layers (Fig. 8a).

325 Like in the HL, the impact on the formation of persistent contrails of switching from kerosene to ethanol or to hydrogen decreases with decreasing pressure in the ML. In this region, with kerosene as fuel, aircraft produce persistent contrails more

frequently (for 16 % of the flight time) in the 275-225 hPa layer (Fig. 8b) which corresponds to the pressure range where aircraft fly most (Fig. 2). This occurrence frequency is about 11.3 % in the 325-275 hPa layer and 9 % in the 225-175 hPa layer (Fig. 8b). Overall, the impact of switching fuel is highest for 325-275 hPa and lowest for 225-175 hPa (Fig. 8b).

330 Persistent contrail occurrence as a function of fuel in the tropics increases with decreasing pressure. More importantly, the impact of switching from kerosene to ethanol or hydrogen is most important at pressure where aircraft fly the most (275-225 hPa) (Fig. 8c and Fig. 2c). At these altitudes, persistent contrails occur 0.7 % of the time with kerosene but would occur 4.0 % and 9.5 % of the time, respectively, with ethanol and hydrogen (Fig. 8c). The change is also important in the 225-175 hPa layer (Fig. 8c).

335 Overall, the differences in the impact of switching from kerosene to ethanol or to hydrogen are driven by temperature variability. The differences are higher in warmer seasons than in the colder seasons (see Table S1 to S3 in the Supplementary Material). At low ambient temperature, the contrail plume exceeds water saturation more readily due to the curvature of the vapour pressure curve, regardless of the fuel being considered. At higher ambient temperatures, the contrail plume may stay subsaturated with respect to liquid water if the ratio of EI_{H_2O} to Q is low. Therefore, persistent contrails are less frequent with 340 kerosene than with hydrogen and ethanol. With the warming of the upper troposphere expected as a result of climate change (Kumar et al., 2022), the impact of switching from kerosene to ethanol or to hydrogen on contrail formation frequency could further increase in the future, potentially affecting pressure layers (e.g., 225-175 hPa in the high and mid-latitudes) and seasons (winter and spring in the high and mid-latitudes) where it is low under present conditions.

345 The frequency of non-persistent contrail formation increases with latitude and with decreasing pressure between 325 and 175 hPa (Fig. 9). At these pressure layers, the impact of switching from kerosene to ethanol or to hydrogen is largest in the tropics (Fig. 9) and in summer, followed by autumn for the three regions (not shown). Our results confirm and generalize those of Wolf et al. (2023) who showed that the impact of switching from kerosene to ethanol or to hydrogen will be greater on the occurrence of non-persistent contrails than on persistent contrails using radiosoundings in the Paris region.

4 Summary and conclusions

350 In the present study, we documented the properties of the atmospheric RHi PDF over the period 1995-2022 using the long-term MOZAIC and IAGOS observations made onboard passenger aircraft. The frequency of the contrail formation conditions is also analysed. The analyses are carried out over the HL and ML regions of the Northern Hemisphere and in the tropics, in the UT and LS. The UT and LS pressure layer (325-175 hPa) is split into three pressure layers with a resolution of 50 hPa. Measurements with ozone volume mixing ratio below 130 ppb were flagged as belonging to the UT, while those with ozone 355 volume mixing ratio above 130 ppb are flagged as LS measurements. RHi PDF properties are also documented in clear sky and in cirrus cloud conditions. We used ice crystal number concentrations thresholds of 0.001, 0.015 and 0.05 particles cm^{-3} for clouds detection. The contrail formation conditions have been detected using the Schmidt-Appleman criterion considering an aircraft-engine propulsion efficiency of 0.3. The main results of our analysis are as follows:

1. The cirrus clouds fraction sampled by IAGOS aircraft depends on the detection threshold and the location. Cirrus clouds
360 are more frequent in the tropics than in the ML and their frequency decreases if a higher detection threshold is chosen. Cirrus clouds are characterized by higher amount of ice supersaturation than clear sky, which shifts the overall RHi PDF towards more ice supersaturation with a peak around 100 %.

2. We characterized the PDF of RHi in the UT. In the HL, the ML and the tropics, the PDF decreases exponentially with
365 increasing RHi in ice supersaturation conditions. In subsaturated conditions, it increases exponentially with RHi in the HL and the ML regions while it decreases exponentially in the tropics. Combining these different shapes of subsaturated RHi PDF in the tropics and in mid and high latitudes (ML and HL) leads to a global tropospheric RHi PDF that follows an almost uniform distribution.

3. The RHi PDF in the LS is different from that in the UT in the HL and ML. It decreases exponentially with increasing
370 RHi in both sub- and supersaturated regions. However, slope of the decrease of the PDF is higher for supersaturated conditions than subsaturated conditions. The combination of these different shapes of subsaturated RHi PDF in the LS and in the UT leads to a bimodal PDF in the ML and in HL.

4. The probability of forming non-persistent and persistent contrails by aircraft using bio-ethanol and liquid-hydrogen instead of kerosene was also analysed. Both are candidate fuels for reducing the climate impact of aviation. We found
375 that these alternative fuels are more likely to produce contrails than kerosene. However, the magnitude of their impact on persistent contrail formation depends on pressure level and latitude. In the HL of the Northern Hemisphere, switching from kerosene to liquid-hydrogen or bio-ethanol has very little impact on the persistent contrails frequency for the 275-225 and 225-175 hPa layers. The reason is that, in the HL of the Northern Hemisphere, aircraft running on kerosene already form persistent contrails nearly every time they encounter air masses that are supersaturated with respect to ice at these altitudes. The same conclusions are found for 225-175 hPa in the ML. Overall, the impact of switching
380 from kerosene to liquid-hydrogen or bio-ethanol on persistent contrail occurrence decreases from tropics to high-latitude regions. It decreases with pressure between 325 and 175 hPa except in the tropics. The impact of switching from kerosene to liquid-hydrogen will be more important for non-persistent contrails.

This study updates and completes some aspects of the studies of Gierens et al. (1999) and Spichtinger et al. (2003a) on the characteristics of the RHi PDF. We draw several recommendations from our study. Comparisons between models and
385 observations need to be performed for UT and LS separately, and preferentially over different regions and pressure levels, distinguishing cloud-free and cloudy conditions. Models that are calibrated to reproduce the global RHi PDF from MOZAIC and IAGOS data may do so for the wrong reasons. Similarly, it is important that observing systems designed to monitor UTLS humidity have the capability to distinguish UT from LS. This may be a challenge for satellite-based systems, which may not have a sufficiently good vertical resolution. Finally, studies on the impact on the contrail occurrence of switching from fossil
390 kerosene to more sustainable fuels must be conducted in various meteorological conditions.

Data availability. IAGOS data are available from the IAGOS data portal (<https://doi.org/10.25326/20>). We use IAGOS data accessed on 3 november 2023.

Author contributions. SS, OB and NB designed the study. SS carried out the analysis and the preparation of the manuscript. OB and AB helped with the analysis. OB, AB, NB, KW contributed to the preparation of the manuscript. SR provided the MOZAIC and IAGOS data.

395 *Competing interests.* The authors declare that they have no conflict of interest.

Acknowledgements. S. Sanogo, O. Boucher, N. Bellouin, A. Borella and K. Wolf acknowledge support from the French Ministère de la Transition écologique (grant no. DGAC 382 N2021-39), with support from France's Plan National de Relance et de Resilience (PNRR) and the European Union's NextGenerationEU. We acknowledge the strong support of the European Commission, Airbus and the airlines (Deutsche Lufthansa, Air France, Austrian, Air Namibia, Cathay Pacific, Iberia, China Airlines, Hawaiian Airlines, Eurowings Discover, and 400 Air Canada) that have carried the MOZAIC or IAGOS equipment and performed the maintenance since 1994. IAGOS has been funded by the European Union projects IAGOS-DS and IAGOS-ERI. Additionally, IAGOS has been funded by INSU-CNRS (France), Météo-France, Université Paul Sabatier (Toulouse, France) and Research Center Jülich (FZJ, Jülich, Germany). The IAGOS database is supported in France by AERIS (<https://www.aeris-data.fr>)

References

405 Appleman, H.: The formation of exhaust condensation trails by jet aircraft, *Bull. Am. Soc.*, 34, 14–20, <https://doi.org/10.1175/1520-0477-34.1.14>, 1953.

Beswick, K., Baumgardner, D., Gallagher, M., Raga, G. B., Minnis, P., Spangenberg, D. A., Volz-Thomas, A., Nedelec, P., and Wang, K.-Y.: Properties of small cirrus ice crystals from commercial aircraft measurements and implications for flight operations, *Tellus B*, 67, 27876, <https://doi.org/10.3402/tellusb.v67.27876>, 2015.

410 Bickel, M.: Climate impact of contrail cirrus, Ph.D. thesis, DLR-Forschungsbericht. DLR-FB-2023-14. Dissertation. Ludwig-Maximilians-Universität München. 133 S., <https://doi.org/10.57676/mzmg-r403>, 2023.

Dekoutsidis, G., Groß, S., Wirth, M., Krämer, M., and Rolf, C.: Characteristics of supersaturation in midlatitude cirrus clouds and their adjacent cloud-free air, *Atmos. Chem. Phys.*, 23, 3103–3117, <https://doi.org/10.5194/acp-23-3103-2023>, 2023.

Diao, M., Zondlo, M. A., Heymsfield, A. J., Avallone, L., Paige, M., Beaton, S., Campos, T., and Rogers, D.: Cloud-scale ice-supersaturated regions spatially correlate with high water vapor heterogeneities, *Atmos. Chem. Phys.*, 14, 2639–2656, <https://doi.org/10.5194/acp-14-2639-2014>, 2014.

415 Duhnke, K., Wefers, J., Speth, P., Kley, D., Marenco, A., and Smit, H. G.: Untersuchung der in MOZAIC gemessenen Ozon-und Wasserdampfverteilung im polaren Strahlstrom über dem Nordatlantik, Tech. rep., Forschungszentrum Jülich, <https://juser.fz-juelich.de/record/864943>, 1998.

420 Genthon, C., Piard, L., Vignon, E., Madeleine, J.-B., Casado, M., and Gallée, H.: Atmospheric moisture supersaturation in the near-surface atmosphere at Dome C, Antarctic Plateau, *Atmos. Chem. Phys.*, 17, 691–704, <https://doi.org/10.5194/acp-17-691-2017>, 2017.

Gierens, K. and Brinkop, S.: Dynamical characteristics of ice supersaturated regions, *Atmos. Chem. Phys.*, 12, 11 933–11 942, <https://doi.org/10.5194/acp-12-11933-2012>, 2012.

425 Gierens, K., Schumann, U., Helten, M., Smit, H., and Marenco, A.: A distribution law for relative humidity in the upper troposphere and lower stratosphere derived from three years of MOZAIC measurements, *Annales Geophysicae*, 17, 1218–1226, <https://doi.org/10.1007/s00585-999-1218-7>, 1999.

Gierens, K., Spichtinger, P., and Schumann, U.: Ice supersaturation, in: *Atmospheric Physics: Background–Methods–Trends*, pp. 135–150, Springer, 2012.

Heymsfield, A., Krämer, M., Luebke, A., Brown, P., Cziczo, D., Franklin, C., Lawson, P., Lohmann, U., McFarquhar, G., Ulanowski, Z., and 430 Van Tricht, K.: Cirrus clouds, *Meteor. Monogr.*, 58, 2.1–62.26, <https://doi.org/10.1175/AMSMONOGRAPH-D-16-0010.1>, 2017.

Kahn, B. H., Gettelman, A., Fetzer, E. J., Eldering, A., and Liang, C. K.: Cloudy and clear-sky relative humidity in the upper troposphere observed by the A-train, *J. Geophys. Res.*, 114, <https://doi.org/10.1029/2009JD011738>, 2009.

Kanji, Z. A., Ladino, L. A., Wex, H., Boose, Y., Burkert-Kohn, M., Cziczo, D. J., and Krämer, M.: Overview of ice nucleating particles, *Meteor. Monogr.*, 58, 1.1–1.33, <https://doi.org/10.1175/AMSMONOGRAPH-D-16-0006.1>, 2017.

435 Kärcher, B.: Formation and radiative forcing of contrail cirrus, *Nat. Commun.*, 9, 1824, <https://doi.org/10.1038/s41467-018-04068-0>, 2018.

Krämer, M., Schiller, C., Afchine, A., Bauer, R., Gensch, I., Mangold, A., Schlicht, S., Spelten, N., Sitnikov, N., Borrmann, S., et al.: Ice supersaturations and cirrus cloud crystal numbers, *Atmos. Chem. Phys.*, 9, 3505–3522, <https://doi.org/10.5194/acp-9-3505-2009>, 2009.

Krämer, M., Rolf, C., Luebke, A., Afchine, A., Spelten, N., Costa, A., Meyer, J., Zoeger, M., Smith, J., Herman, R. L., et al.: A microphysics guide to cirrus clouds–Part 1: Cirrus types, *Atmos. Chem. Phys.*, 16, 3463–3483, <https://doi.org/10.5194/acp-16-3463-2016>, 2016.

440 Kumar, T. L., Durga, G. P., Aravindhavel, A., Barbosa, H., and Rao, D. N.: Analysis of tropospheric warming and stratospheric cooling in the present and future climate from the suite of CMIP6 models, *Theor Appl Climatol*, 149, 1717–1726, <https://doi.org/10.1007/s00704-022-04136-y>, 2022.

445 Lamquin, N., Stubenrauch, C., Gierens, K., Burkhardt, U., and Smit, H.: A global climatology of upper-tropospheric ice supersaturation occurrence inferred from the Atmospheric Infrared Sounder calibrated by MOZAIC, *Atmos. Chem. Phys.*, 12, 381–405, <https://doi.org/10.5194/acp-12-381-2012>, 2012.

450 Lee, D. S., Fahey, D. W., Skowron, A., Allen, M. R., Burkhardt, U., Chen, Q., Doherty, S. J., Freeman, S., Forster, P. M., Fuglestvedt, J., et al.: The contribution of global aviation to anthropogenic climate forcing for 2000 to 2018, *Atmos. Environ.*, 244, 117834, <https://doi.org/10.1016/j.atmosenv.2020.117834>, 2021.

455 Li, Y., Mahnke, C., Rohs, S., Bundke, U., Spelten, N., Dekoutsidis, G., Groß, S., Voigt, C., Schumann, U., Petzold, A., et al.: Upper tropospheric slightly ice-subsaturated regions: frequency of occurrence and statistical evidence for the appearance of contrail cirrus, *Atm. Chem. Phys.*, 23, 2251–2271, <https://doi.org/10.5194/acp-23-2251-2023>, 2023.

460 Liu, Y., Xu, T., and Liu, J.: Characteristics of the seasonal variation of the global tropopause revealed by COSMIC/GPS data, *Advances in space research*, 54, 2274–2285, <https://doi.org/10.1016/j.asr.2014.08.020>, 2014.

465 Lloyd, G., Gallagher, M., Choularton, T., Krämer, M., Andreas, P., and Baumgardner, D.: In situ measurements of cirrus clouds on a global scale, *Atmosphere*, 12, 41, <https://doi.org/10.3390/atmos12010041>, 2020.

Marengo, A., Thouret, V., Nédélec, P., Smit, H., Helten, M., Kley, D., Karcher, F., Simon, P., Law, K., Pyle, J., et al.: Measurement of ozone and water vapor by Airbus in-service aircraft: The MOZAIC airborne program, An overview, *Journal of Geophysical Research: Atmospheres*, 103, 25 631–25 642, <https://doi.org/10.1029/98JD00977>, 1998.

470 Ng, K. S., Farooq, D., and Yang, A.: Global biorenewable development strategies for sustainable aviation fuel production, *Renewable and Sustainable Energy Reviews*, 150, 111 502, <https://doi.org/10.1016/j.rser.2021.111502>, 2021.

Ovarlez, J., Gayet, J.-F., Gierens, K., Ström, J., Ovarlez, H., Auriol, F., Busen, R., and Schumann, U.: Water vapour measurements inside cirrus clouds in Northern and Southern hemispheres during INCA, *Geophys. Res. Lett.*, 29, 60–1, <https://doi.org/10.1029/2001GL014440>, 2002.

Peixoto, J. P. and Oort, A. H.: Physics of climate, 1992.

475 Petzold, A., Thouret, V., Gerbig, C., Zahn, A., Brenninkmeijer, C. A., Gallagher, M., Hermann, M., Pontaud, M., Ziereis, H., Boulanger, D., et al.: Global-scale atmosphere monitoring by in-service aircraft—current achievements and future prospects of the European Research Infrastructure IAGOS, *Tellus B*, 67, 28 452, <https://doi.org/10.3402/tellusb.v67.28452>, 2015.

Petzold, A., Krämer, M., Neis, P., Rolf, C., Rohs, S., Berkes, F., Smit, H. G., Gallagher, M., Beswick, K., Lloyd, G., et al.: Upper tropospheric water vapour and its interaction with cirrus clouds as seen from IAGOS long-term routine in situ observations, *Faraday Discussions*, 200, 229–249, 2017.

480 Petzold, A., Neis, P., Rütimann, M., Rohs, S., Berkes, F., Smit, H. G., Krämer, M., Spelten, N., Spichtinger, P., Nédélec, P., et al.: Ice-supersaturated air masses in the northern mid-latitudes from regular in situ observations by passenger aircraft: Vertical distribution, seasonality and tropospheric fingerprint, *Atmos. Chem. Phys.*, 20, 8157–8179, <https://doi.org/10.5194/acp-20-8157-2020>, 2020.

Ponater, M., Bickel, M., Bock, L., and Burkhardt, U.: Towards determining the contrail cirrus efficacy, *Aerospace*, 8, 42, <https://doi.org/10.3390/aerospace8020042>, 2021.

485 Rap, A., Forster, P., Jones, A., Boucher, O., Haywood, J., Bellouin, N., and De Leon, R.: Parameterization of contrails in the UK Met Office climate model, *J. Geophys. Res.*, 115, <https://doi.org/10.1029/2009JD012443>, 2010.

Reutter, P., Neis, P., Rohs, S., and Sauvage, B.: Ice supersaturated regions: properties and validation of ERA-Interim reanalysis with IAGOS in situ water vapour measurements, *Atmos. Chem. Phys.*, 20, 787–804, <https://doi.org/10.5194/acp-20-787-2020>, 2020.

480 Sahoo, S., Zhao, X., and Kyprianidis, K.: A review of concepts, benefits, and challenges for future electrical propulsion-based aircraft, *Aerospace*, 7, 44, <https://doi.org/10.3390/aerospace7040044>, 2020.

Schmidt, E.: Die entstehung von eisnebel aus den auspuffgasen von flugmotoren, *Schriften der Deutschen Akademie der Luftfahrtforschung*, Verlag R. Oldenbourg, München, Heft 44, 5, 1–15, 1941.

Schumann, U.: On conditions for contrail formation from aircraft exhausts, *Meteorologische Zeitschrift*, 5, 4–23, 485 <https://doi.org/10.1127/metz/5/1996/4>, 1996.

Schumann, U.: A contrail cirrus prediction model, *Geosci. Model Dev.*, 5, 543–580, <https://doi.org/10.5194/gmd-5-543-2012>, 2012.

Schumann, U., Bugliaro, L., Dörnbrack, A., Baumann, R., and Voigt, C.: Aviation contrail cirrus and radiative forcing over Europe during 6 months of COVID-19, *J. Geophys. Res.*, 48, e2021GL092771, <https://doi.org/10.1029/2021GL092771>, 2021.

Smit, H. G., Rohs, S., Neis, P., Boulanger, D., Krämer, M., Wahner, A., and Petzold, A.: Reanalysis of upper troposphere humidity data from 490 the MOZAIC programme for the period 1994 to 2009, *Atmos. Chem. Phys.*, 14, 13 241–13 255, <https://doi.org/10.5194/acp-14-13241-2014>, 2014.

Sourdeval, O., Gryspeerdt, E., Krämer, M., Goren, T., Delanoë, J., Afchine, A., Hemmer, F., and Quaas, J.: Ice crystal number concentration estimates from lidar–radar satellite remote sensing – Part 1: Method and evaluation, *Atmos. Chem. Phys.*, 18, 14 327–14 350, <https://doi.org/10.5194/acp-18-14327-2018>, 2018.

495 Sperber, D. and Gierens, K.: Towards a more reliable forecast of ice supersaturation: concept of a one-moment ice-cloud scheme that avoids saturation adjustment, *Atmos. Chem. Phys.*, 2023, 1–23, <https://doi.org/10.5194/acp-23-15609-2023>, 2023.

Spichtinger, P., Gierens, K., Leiterer, U., and Dier, H.: Ice supersaturation in the tropopause region over Lindenberg, Germany, *Meteorologische Zeitschrift*, 12, 143–156, <https://doi.org/10.1256/qj.02.141>, 2003a.

Spichtinger, P., Gierens, K., and Read, W.: The global distribution of ice-supersaturated regions as seen by the Microwave Limb Sounder, *Q. 500 J. R. Meteorol Soc.*, 129, 3391–3410, <https://doi.org/10.1256/qj.02.141>, 2003b.

Wolf, K., Bellouin, N., and Boucher, O.: Long-term upper-troposphere climatology of potential contrail occurrence over the Paris area derived from radiosonde observations, *Atmos. Chem. Phys.*, 23, 287–309, <https://doi.org/10.5194/acp-23-287-2023>, 2023.